Inorganic Chemistry
Article
pubs.acs.org/IC

$BaFe_9LiO_{15}$: A New Layered Antiferromagnetic Ferrite

Tao Yang,[†] Aziz Daoud-Aladine,[‡] Michael F. Thomas,[§] John B. Claridge,*,[†] and Matthew J. Rosseinsky*,[†]

[†]Department of Chemistry, University of Liverpool, Liverpool L69 7ZD, United Kingdom
[‡]ISIS Facility, Rutherford Appleton Laboratory, Harwell, Didcot OX11 0DE, United Kingdom
[§]Department of Physics, University of Liverpool, Liverpool L69 7ZE, United Kingdom

Supporting Information

ABSTRACT: The new Fe^{3+} oxide $BaFe_9LiO_{15}$ is isostructural with the magnetically frustrated material $BaV_{10}O_{15}$, adopting a structure based on the stacking of close-packed pure oxide and BaO_7 layers. Neutron diffraction and Mössbauer spectroscopy shows that $BaFe_9LiO_{15}$ is long-range antiferromagnetically ordered with a Néel temperature of 460 K. The magnetic ordering of antiferromagnetically coupled ferromagnetic planes is stabilized by 90° and 180° superexchange interactions between the Fe^{3+} cations that supersede the frustrated in-plane direct exchange observed in t_{2g}-only systems.

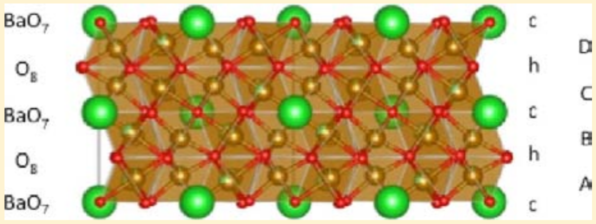

INTRODUCTION

Much attention has been paid to the search for magnetoelectric (ME) multiferroic materials in the past decade.[1−7] For use in practical applications, a magnetic insulator with a high magnetic ordering temperature is extremely desirable. Thus, Fe^{3+}-based oxides (ferrites) are promising candidates, as these materials usually possess both high magnetic ordering temperatures and insulating properties and have long been used in technological applications such as permanent magnet and high-frequency devices.[8−10] The hexaferrites, initially studied by workers at Philips as ferromagnets,[10] make up a large and structurally diverse family of materials described in terms of the stacking of R, S, and T blocks as exemplified in Figure 1. Among these, M, Y, and Z ferrites are the most well-studied; however, many other stacking sequences have been observed, including some with very long periods.[11−14] The hexaferrites are based on close-packed oxide and BaO_3 layers (Figure S1 of the Supporting Information), where Ba^{2+} replaces an oxide anion, and have transition metals in octahedral and tetrahedral environments.

Recently, interesting ME effects have been reported for Y-type ($Ba_{0.5}Sr_{1.5}Zn_2Fe_{12}O_{22}$ and $Ba_2Mg_2Fe_{12}O_{22}$) and Z-type ($Sr_3Co_2Fe_{24}O_{41}$) materials.[15−19] $Ba_{0.5}Sr_{1.5}Zn_2Fe_{12}O_{22}$ has a nonpolar spiral magnetic structure at zero field; via application of an external field perpendicular to the *c*-axis below 130 K, it is converted into a polar cycloid phase.[19] In $Ba_2Mg_2Fe_{12}O_{22}$, a proper screw magnetic structure below 195 K and a longitudinal conical magnetic structure below 50 K transform to a slanted conical spin structure after application of a weak magnetic field (30 mT), which produces detectable ferroelectric polarization.[18] $Sr_3Co_2Fe_{24}O_{41}$ prepared under an oxygen atmosphere is highly resistive at room temperature, and it shows detectable nonlinear ME effects with weak magnetic fields.[15]

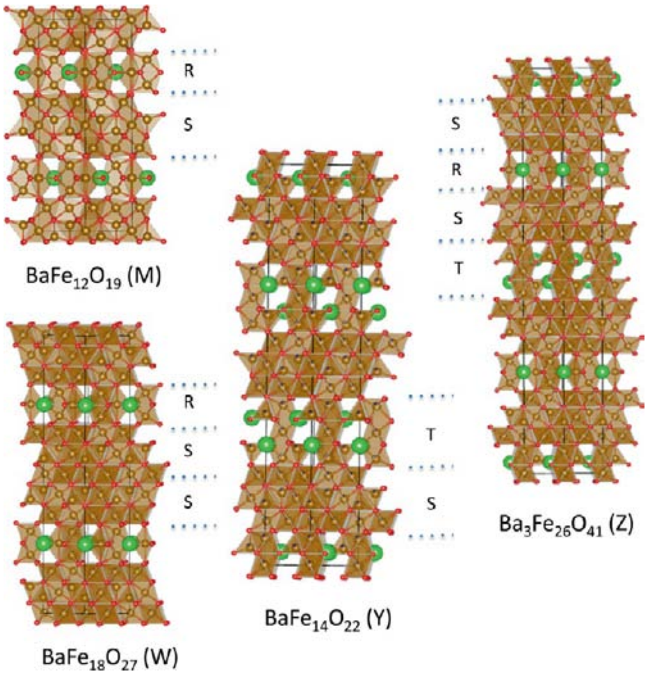

Figure 1. Structures of M, W, Y, and Z ferrites viewed along (110). The stacking repeats in terms of the S, R, and T subunits are shown beside the structures. Green spheres represent barium cations, red spheres oxide anions, and brown spheres iron; iron coordination polyherdra are also colored brown.

The identification of new ferrites thus represents a promising avenue of research. The $BaO-Li_2O-Fe_2O_3$ system is surprisingly underinvestigated, with the W ferrite $BaFe_{17}LiO_{27}$ being the only reported compound.[20] Here we present the synthesis,

Received: November 7, 2012
Published: April 22, 2013

dx.doi.org/10.1021/ic302433a | *Inorg. Chem.* 2013, 52, 4866−4872

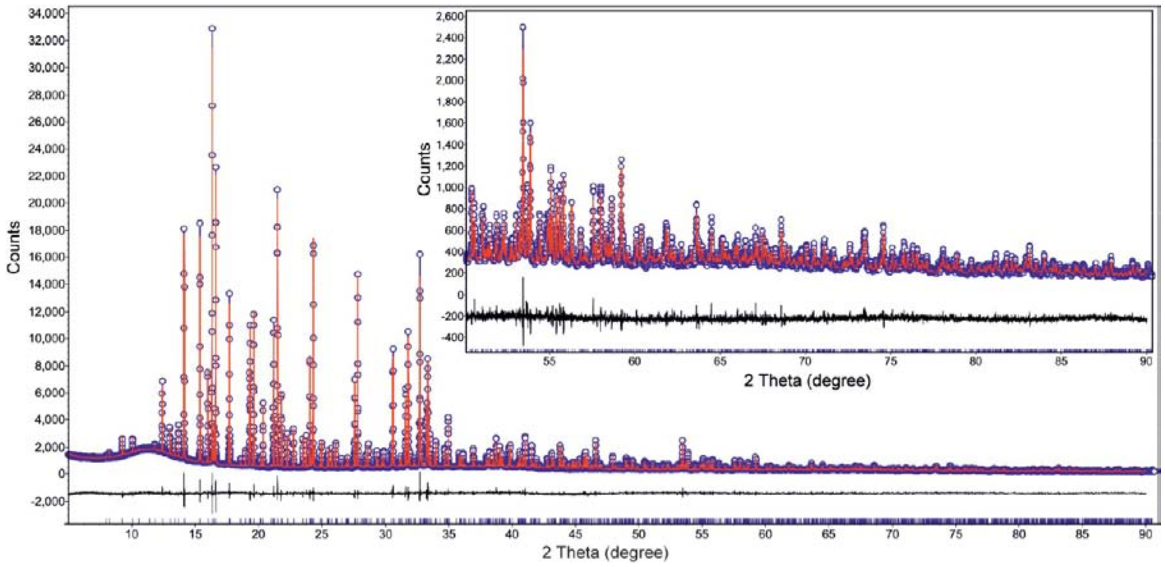

Figure 2. Rietveld refinement plot for $BaFe_9LiO_{15}$ against synchrotron PXRD. The blue circles represent observed data, and the red solid line is the calculated pattern; the marks below the diffraction patterns are the expected reflection positions, and the difference curve is also colored black. The inset is a close-up of the high angle fit.

structure, and magnetic properties of the new ferrite $BaFe_9LiO_{15}$, based on close-packed oxide and BaO_7 layers.

EXPERIMENTAL SECTION

The $BaFe_9LiO_{15}$ phase was identified as part of an investigation of the Ba−Fe−Li−O phase field. Powder samples of $BaFe_9LiO_{15}$ (5 g) were prepared by reaction in air of stoichiometric quantites of $BaCO_3$ (Alfa Aesar, 99.95%), Fe_2O_3 (Puratronic, 99.998%), and Li_2CO_3 (Puratronic, 99.998%), which had been ground thoroughly by hand and pressed into a 13 mm pellet. An initial 10 h calcination at 900 °C was performed to decompose the carbonate; thereafter, the sample was heated at the following temperatures and times, with intermediate grindings: 900 °C for 10 h, 925 °C for 20 h, 925 °C for 20 h, 950 °C for 40 h, 950 °C for 40 h, and 960 °C for 70 h. The annealed samples are monitored by powder XRD, and the minor impurity is M ferrite ($BaFe_{12}O_{19}$-type ferrite) or $BaFe_2O_4$. Thus, before the final heating at 960 °C, 14 mg of Li_2CO_3 was added to remove the impurities.

Lab powder XRD was performed on a Panalytical X'PertPro diffractometer using an X'Celerator detector and Co $K\alpha_1$ radiation (λ = 1.78901 Å) in Bragg−Brentano geometry. Synchrotron powder XRD data were collected at station I11 of the Diamond Light Source (λ = 0.825988 Å) at room temperature, Rietveld refinements were performed using TOPAS.[21] Time of flight (TOF) neutron diffraction data were collected on the GEM instrument at the ISIS facility located at Rutherford Appleton Laboratory. Rietveld refinement of the GEM data was performed using the Fullprof suite.[22] The variable-temperature ^{57}Fe Mössbauer spectra were recorded with a constant acceleration spectrometer. The ^{57}Fe Mössbauer chemical isomer shift data are quoted relative to metallic iron at room temperature. Structures were visualized using VESTA.[23]

RESULTS AND DISCUSSION

Indexing of the X-ray powder diffraction gave a C-centered orthorhombic cell with dimensions of 11.51 Å × 10.22 Å × 9.42 Å. This cell indicates that $BaFe_9LiO_{15}$ is isostructural with other reported $AB_{10}O_{15}$ compounds ($BaCr_{10}O_{15}$, $SrCr_{10}O_{15}$, $BaNi_2Cr_8O_{15}$, $SrNi_2Cr_8O_{15}$, $BaV_{10}O_{15}$, $BaTiV_9O_{15}$, $BaNi_2Sc_8O_{15}$, and $BaNi_2In_8O_{15}$) that adopt space group *Cmca*.[24−32] The structure was refined by the Rietveld method against synchrotron XRD data (Figure 2 and Table 1). There are one Ba, three Fe/Li, and six O crystallographically distinct sites. Atomic coordinates (Table 2), bond distances (Table 3), and angles are provided (Table S1 of the Supporting Information). Free refinement of the Fe/Li site occupancies subject to the constraint of 100% site occupancy places the large majority of the lithium onto the Fe1 position [$BaFe_{8.83(1)}Li_{1.17(1)}O_{15}$]; given the experimental precision in the following, the lithium will be treated as if it was all on the Fe1 site.

Table 1. Refinement and Fit Parameters for $BaFe_9LiO_{15}$

radiation	synchrotron X-ray
sample color	brown
formula mass	886.93
λ (Å)	0.825988
2θ (deg)	4−90
step size	0.005
space group	*Cmca* (No. 64)
a (Å)	11.51020(5)
b (Å)	10.21829(5)
c (Å)	9.42259(4)
V (Å^3)	1108.234(9)
Z	4
ρ_{calcd} (g/cm^3)	5.32
R_p	0.0436
R_{wp}	0.0571
goodness of fit	1.482

$BaFe_9LiO_{15}$ can be regarded as a close-packed layer structure (Figure 3) similar to the ferrites discussed in the Introduction; the structure is described as layered because of the existence of a unique stacking axis for the key structural motifs, although the bonding is not heavily anisotropic. The similar ionic radii of Ba^{2+} and O^{2-} permit the formation of mixed BaO_x close-packed layers in these materials; here Ba^{2+} substitutes at one of eight of the oxide sites in every other O^{2-} layer perpendicular to the *c*-direction to form a BaO_7 layer (Figure 3a). The O_8 and BaO_7 layers stack alternately along the *c*-axis, forming an $(hc)^2$ close-packed sequence in which the O_8 layer is hexagonally stacked with respect to the two neighboring BaO_7 layers (Figure 3a). There are two BaO_7 layers in the unit cell with the Ba positions related by in-plane C centring to maximize the separation of the

Table 2. Refined Atomic Parameters from Synchrotron X-ray Diffraction Refinement [refined composition of $BaFe_{8.83(1)}Li_{1.17(1)}O_{15}$]

atom	site	x	y	z	U_{eq} (Å^2)	occupancy	BVS
Ba	4b	0	0.5	0	0.019(1)	1	2.014
Fe1	16g	0.26172(8)	0.16077(9)	0.1138(1)	0.005(1)	0.739(2)	2.882
Li1						0.261(2)	1.305
Fe2	8f	0	0.1850(1)	0.1366(1)	0.003(1)	0.990(3)	2.805
Li2						0.010(3)	1.272
Fe3	16g	0.37028(7)	0.41436(7)	0.14665(7)	0.003(1)	0.974(3)	2.885
Li3						0.026(3)	1.307
O1	8e	0.25	0.3224(4)	0.25	0.003(2)	1	2.046
O2	4a	0.5	0	0.5	0.012(2)	1	1.648
O3	8d	0.7440(4)	0.5	0	0.001(1)	1	2.087
O4	16g	0.8727(3)	0.4125(3)	0.7439(3)	0.003(1)	1	2.072
O5	16g	0.1258(3)	0.2359(3)	0.9966(4)	0.001(1)	1	2.076
O6	8f	0	0.6544(4)	0.7591(5)	0.001(1)	1	2.093

Table 3. Selected Bond Distances (angstroms) in $BaFe_9LiO_8$ from Synchrotron X-ray Diffraction Refinement

bond	length	bond	length	bond	length	bond	length
Ba−O6 × 2	2.765(5)	Fe1−O5	1.968(3)	Fe2−O6	1.913(5)	Fe3−O1	1.936(2)
Ba−O3 × 2	2.947(4)	Fe1−O3	1.973(1)	Fe2−O5 × 2	2.027(3)	Fe3−O6	1.961(3)
Ba−O4 × 4	2.961(3)	Fe1−O4	1.997(3)	Fe2−O4 × 2	2.040(3)	Fe3−O4	1.993(3)
Ba−O5 × 4	3.062(3)	Fe1−O5	2.064(3)	Fe2−O2	2.287(1)	Fe3−O5	2.045(3)
		Fe1−O1	2.096(3)			Fe3−O3	2.099(3)
		Fe1−O4	2.111(4)			Fe3−O2	2.2146(8)
		average	2.035	average	2.056	average	2.041
		distortion	0.073	distortion	0.196	distortion	0.144

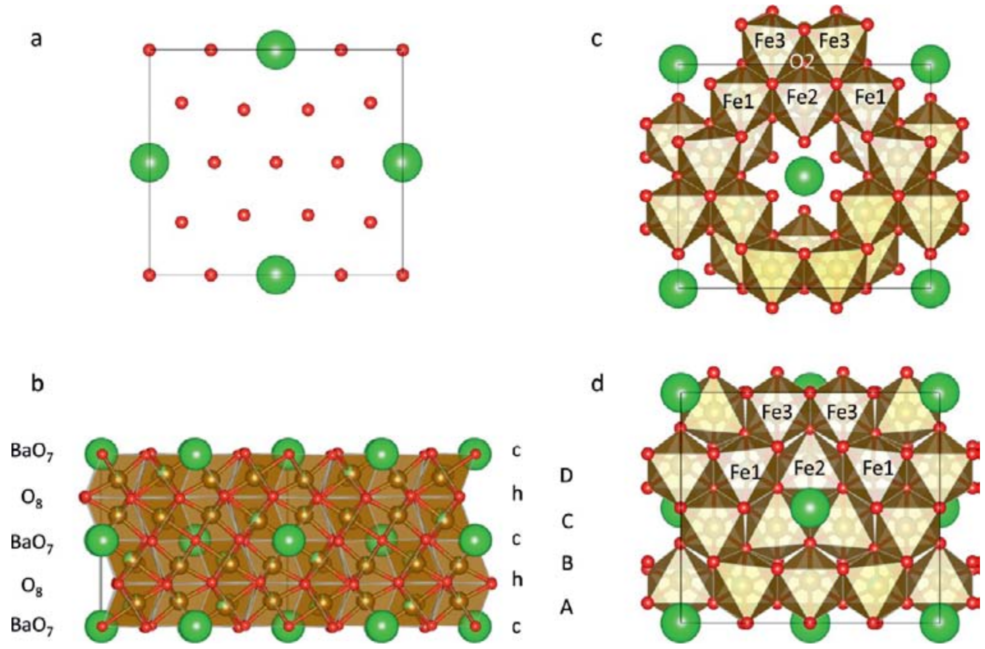

Figure 3. (a) BaO_7 layer viewed down the c-axis. (b) Layered stacking of close-packed BaO_7 and O_8 layers in $BaFe_9LiO_{15}$, viewed along the a-axis. The close-packed layers are stacked in an $(hc)^2$ repeat along the c-axis, and the four distinct octahedral metal layers are labeled A−D. (c) View of the cubic layer along the c-axis (c, BaO_7 layer with adjacent B and C layers). The underbonded O2 anion that forms part of three shared edges within the layer of octahedral interstitial sites is indicated. (d) View of the hexagonal layer along the c-axis (h, O_8 layer with adjacent A and B layers). Green spheres represent barium cations, red spheres oxide anions, and brown spheres iron, and iron coordination polyhedra are also colored brown.

Ba^{2+} cations. The Fe^{3+} cations occupy octahedral interstitial sites between these layers. The resulting layers of interstitial sites are termed A−D, which is significant in the discussion of the magnetic structure. Electrostatic forces preclude the occupation of the octahedral interstitial sites adjacent to Ba^{2+}. As shown in panels b and c of Figure 3, only five of eight of the octahedral sites are therefore occupied to give an $AB_{10}O_{15}$ formula, where Fe^{3+} and Li^+ co-occupy one of the B sites. There are two qualitatively distinct sets of octahedral sites in a 2:1 ratio, the Fe2 site being adjacent to the empty sites produced by the Ba^{2+} cation (Figure

Table 4. M−M Distances (angstroms) and Connection Types for $BaFe_9LiO_{15}$

M−M	distance	connection	bridge	M−M	distance	connection	bridge
Fe1−Fe1	2.580(2)	face	O1, O4, O4	Fe3−Fe1	2.893(1)	edge	O1, O5
Fe1−Fe1	2.829(2)	edge	O5, O5	Fe3−Fe1	2.957(1)	edge	O3, O4
Fe1−Fe3	2.893(1)	edge	O1, O5	Fe3−Fe3	2.986(2)	edge	O2, O6
Fe1−Fe3	2.957(1)	edge	O3, O4	Fe3−Fe1	2.987(1)	edge	O3, O5
Fe1−Fe3	2.987(1)	edge	O3, O5	Fe3−Fe2	3.144(1)	edge	O2, O4
Fe1−Fe2	3.0302(9)	edge	O4, O5	Fe3−Fe2	3.222(1)	edge	O2, O5
Fe1−Fe3	3.605(1)	corner	O4	Fe3−Fe3	3.271(1)	edge	O2, O3
Fe1−Fe2	3.621(1)	corner	O4	Fe3−Fe3	3.385(2)	corner	O1
Fe1−Fe3	3.757(1)	corner	O1	Fe3−Fe2	3.449(1)	corner	O6
Fe1−Fe1	3.924(2)	corner	O3	Fe3−Fe1	3.605(1)	corner	O4
Fe1−Fe2	3.947(1)	corner	O5	Fe3−Fe1	3.757(1)	corner	O1
Fe2−Fe1 × 2	3.0302(9)	edge	O4, O5				
Fe2−Fe3 × 2	3.144(1)	edge	O2, O4				
Fe2−Fe3 × 2	3.222(1)	edge	O2, O5				
Fe2−Fe3 × 2	3.449(1)	corner	O6				
Fe2−Fe1 × 2	3.621(1)	corner	O4				
Fe2−Fe1 × 2	3.947(1)	corner	O5				

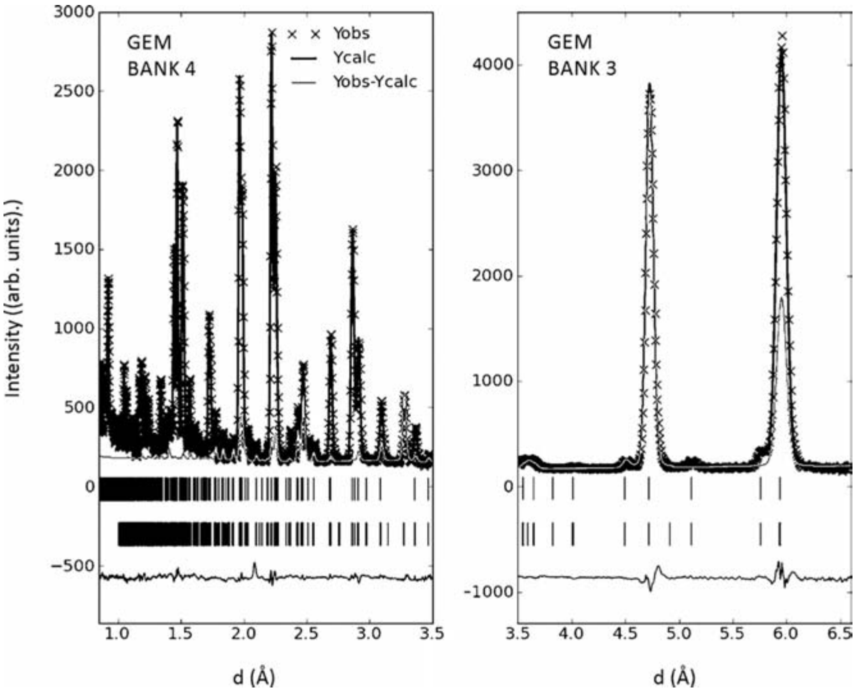

Figure 4. Magnetic Rietveld refinement plot for $BaFe_9LiO_{15}$ against banks 2−5 (only banks 3 and 4 are shown) of GEM. The black crosses represent observed data, and the black solid line is the calculated pattern and the gray solid line the magnetic contribution; the top set of tick marks are for the nuclear Bragg peaks and the bottom set for the magnetic Bragg peaks. The difference curve is also colored black (bank 3, R_{wp} = 3.07%, Bragg R factor of 3.22%, magnetic R factor of 1.44%; bank 4, R_{wp} = 2.44%, Bragg R factor of 2.62%, magnetic R factor of 4.67%).

3c). On either side of the O_8 (h) layer, there are face-sharing $Fe1O_6$ octahedra (Figure 3c) with a short metal−metal distance of 2.580(2) Å. The ordering of the lower-charge Li^+ cation on this site weakens the electrostatic repulsions between the face-shared cations. The cation bond valence sums (BVS) are close to those expected for the formal oxidation states. O2 is underbonded in comparison with the other oxide anions and also has a higher displacement parameter. This oxide anion is the only one that bridges three iron (Fe2/Fe3, not the Li^+-containing Fe1) sites by participating in three shared edges, and the underbonding can be assigned to displacements of the Fe cations from this multiply shared oxide toward the empty octahedral sites arising because of the Ba^{2+} cation.

This is consistent with the observed distortion of the three octahedral sites. The average Fe−O bond lengths for Fe1−Fe3 are very similar. The three FeO_6 octahedra all show distortions (Table 3) that are largest for Fe2 and Fe3, both of which have strongly elongated bonds to O2 reflecting the displacement noted above. The FeO_6 octahedra are connected as listed in Table 4. $Fe1O_6$ shares a common face with another $Fe1O_6$ octahedron via O1, O4, and O4. $Fe1O_6$ shares its edges with one neighboring $Fe1O_6$, one $Fe2O_6$, and three $Fe3O_6$ octahedra, with the Fe−Fe distances in the range of 2.829(2)−3.0302(9) Å, ∼0.3 Å longer than the face-sharing contacts. $Fe1O_6$ shares corners with a further five octahedra. Fe2 is located on an inversion center, and thus, the $Fe2O_6$ octahedron shares edges with six

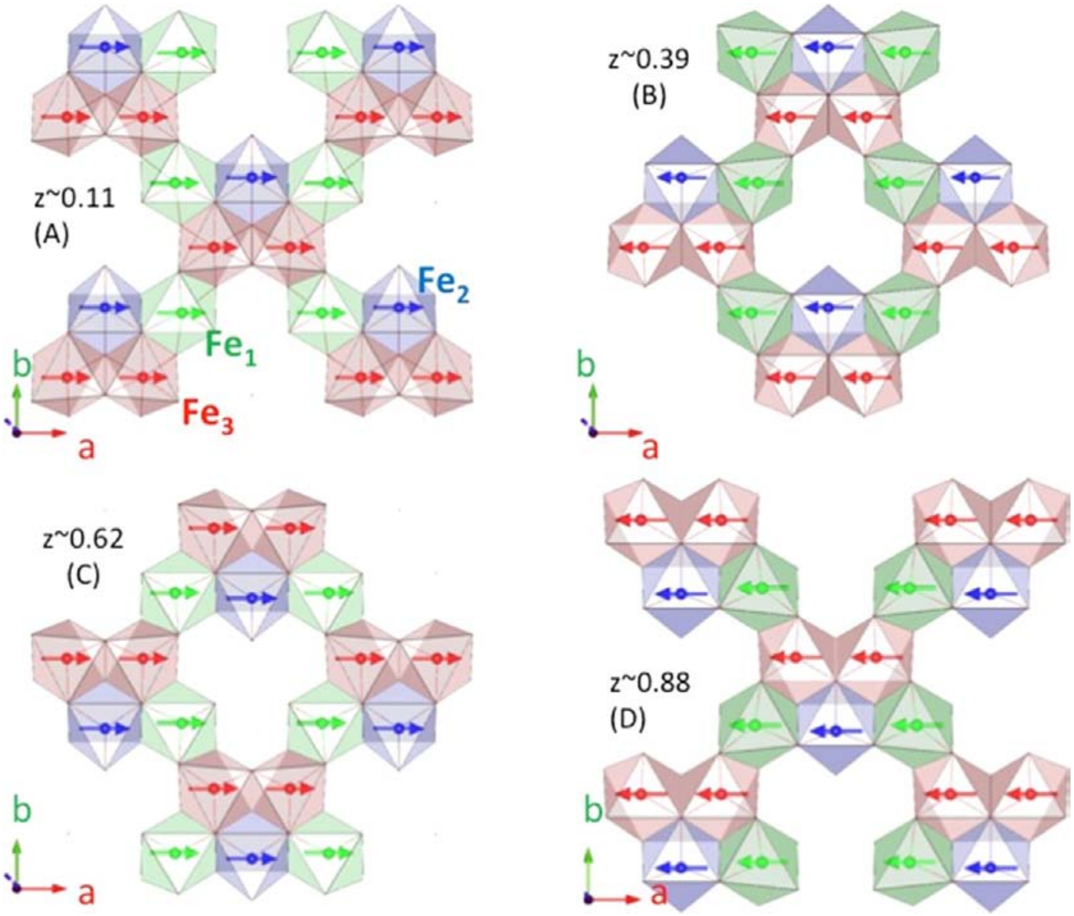

Figure 5. Magnetic structure of $BaFe_9LiO_{15}$ viewed in terms of ferromagnetic octahedral layers viewed along the *c*-axis stacked antiferromagnetically.

neighboring octahedra and shares corners with six other octahedra. $Fe3O_6$ shares edges with seven octahedra and corners with four.

Strong magnetic Bragg peaks are observed in the room-temperature neutron diffraction data that can be indexed with a propagation vector $\mathbf{k}$ = (0,0,0) (Figure 4). Representational analysis was conducted using Bassirep within the Fullprof suite,[22] yielding eight possible representations based on magnetic moments at the Fe^{3+} sites. (Table S2 of the Supporting Information). All possibilities were tested. For all sites, only putting magnetic modes along the *a*-axis projected out from the GM4-irreducible representation yielded satisfactory fits to the data. Refinement of additional components with moments along the *b*- and *c*-axes gives zero moment values within the standard deviations but does not improve the fit. The structure is therefore refined with all spins collinear along the *a*-axis, yielding moments of 3.29(6), 3.34(11), and 3.29(5) μ_B for Fe1−Fe3, respectively (Figure 5), which is slightly lower than the values of 3.96 μ_B calculated for the Brillouin function for a T_N/T of 1.55. This structure can be viewed as ferromagnetic sheets stacked antiferromagnetically (Figure 6).

The crystal structure has an intricate and complex arrangement of edge-, corner-, and face-sharing FeO_6 octahedra. The examination of the Fe−O−Fe bonding suggests a possible competition on some pairs of sites (discussed below), between ~90° and ~180° superexchange interactions, expected to be ferromagnetic (FM) and antiferromagnetic (AFM), respectively, for d^5−d^5 superexchange. The presence of these competing interactions has been shown to frustrate antiferromagnetic ordering in the t_{2g}-based materials $BaV_{10}O_{15}$ and $BaCr_{10}O_{15}$.[27] The actual magnetic structure of $BaLiFe_9O_{15}$ turns out to be remarkably simple, with ferromagnetic ordering of Fe moments in the *a*−*b* planes that couple antiferromagnetically along the *c*-axis.

This observation allows us to consider hierarchies of magnetic interactions. The observed FM superexchange within the *a*−*b* plane is assigned to the ~90° superexchange pathways between the edge-shared octahedra. The ferromagnetic in-plane interactions are distinct from the dominant antiferromagnetic interactions found in the t_{2g}-based materials $BaV_{10}O_{19}$ and $BaCr_{10}O_{19}$,[27] where direct exchange appears to be more important, and remove any potential effect of magnetic frustration. The AFM arrangement between the FM planes results from a competition of interactions. Between pairs of adjacent planes of interstitial sites (A and B, and C and D) separated by the h-stacked O_8 layer, the $Fe1O_6$ octahedra share faces, while the remaining octahedra share only corners, producing ~120° superexchange Fe−O−Fe paths due to the h stacking around this layer. These interactions are not expected to be strong. The Fe3−O1−Fe1 angle is 137° and likely to give net antiferromagnetic superexchange (Figure 6a,c). The AFM arrangement therefore results from a strong direct exchange between Fe1 pairs and this superexchange interaction.

Between pairs of adjacent planes (B and C, and D and A), only superexchange interactions (both ~90° and ~180°) are involved (c stacking), depending on whether the octahedra in adjacent layers share corners or edges; ~180° paths across corners are expected to be AFM (Fe1−O3−Fe1, Fe1−O5−Fe2) (Figure

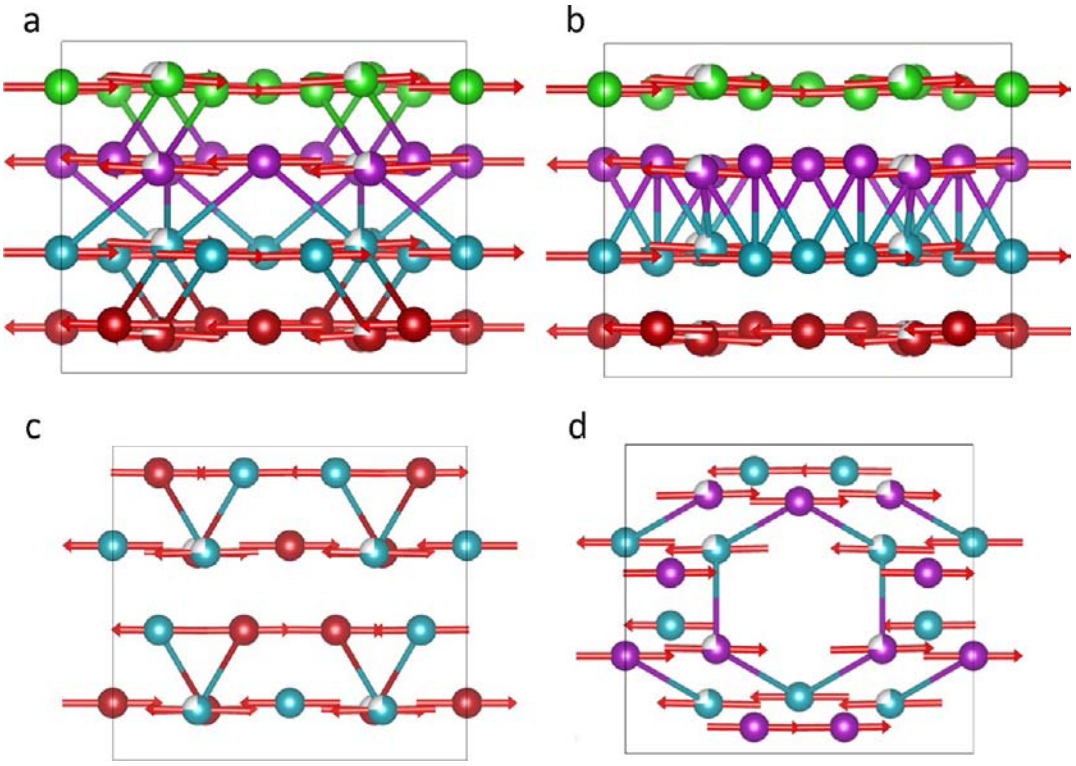

Figure 6. Magnetic structure of $BaFe_9LiO_{15}$. (a) Viewed along the *a*-axis with interlayer near 180° superexchange pathways (>160°, 3.7 Å) via corner sharing octahedra. (b) Viewed along the *a*-axis with interlayer near 90° superexchange pathways via edge sharing octahedra. (c) View of the antiferromagnetic exchange interactions between layers A and B via the O_8 layer. (d) View of the antiferromagnetic exchange interactions between layers B and C via the BaO_7 layer. Dark red, pale blue, purple, and green spheres are irons in layers A–D, respectively; red arrows denote magnetic moment bariums, and oxygens were omitted for the sake of clarity.

6a,d), and ~90° paths across octahedral edges are expected to be FM (Fe1–O3,5–Fe3, Fe2–O2,5–Fe3, Fe1–O5–Fe2, Fe3–O2,3–Fe3) (Figure 6b), like the coupling within the *a*–*b* plane. The observation that the actual arrangement is AF indicates that the ~180° superexchange is stronger, as expected from the first-order nature of the coupling, thereby dominating the ~90° superexchange between edge-sharing FeO_6 octahedra along the *c*-axis. The inter layer network of ~180° superexchange pathways is shown in Figure 6.

The powder neutron data show that there are very strong antiferromagnetic interactions between the Fe^{3+} centers giving AFM ordering above room temperature. Consequently, given the complexities inherent in direct measurement of the magnetic properties due to the presence of even trace high-magnetization parasitic impurities such as the ferromagnetic ferrites (M ferrite or Y ferrite), temperature-dependent ^{57}Fe Mössbauer spectra were collected (Figure S2 of the Supporting Information). The Mössbauer patterns were collected between 500 and 77 K. The fitted parameters are listed in Table S3 of the Supporting Information. The chemical shifts at all temperatures are typical for trivalent iron. It is apparent that T_N is approximately 460 K, below which the spectra are well fit by two types of iron environments with a 2:1 ratio. As shown in Figure 7, the hyperfine fields show expected variation with temperature for both sets of iron ions. By comparison with the crystal structure, a 2:1 ratio matches the (Fe2 + Fe3):Fe1 site ratio, which is also consistent with the larger quadrupole splitting for Fe2 and Fe3 relative to Fe1 because of their more distorted octahedra.

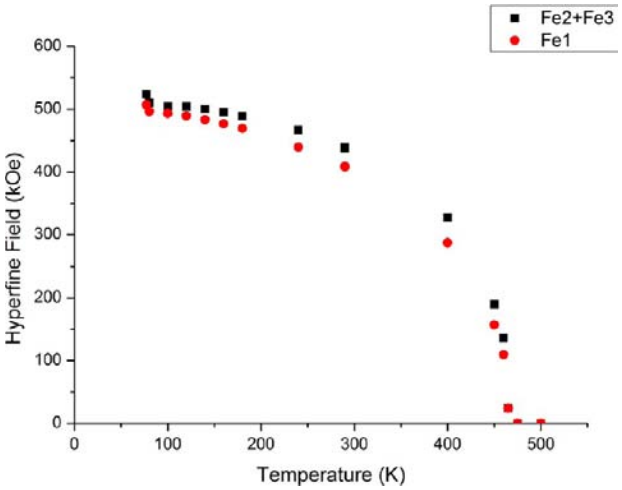

Figure 7. Evolution of the hyperfine field from the Mössbauer spectra of $BaFe_9LiO_{15}$ with temperature.

■ CONCLUSIONS

$BaFe_9LiO_{15}$ is a new Fe^{3+} ferrite, which is isostructural with $BaV_{10}O_{15}$,[33] with an $(hc)^2$ stacking of alternating O_8 and BaO_7 layers, in which all the pure oxygen interstitial sites are filled with iron or lithium. In contrast to the hexaferrites, only octahedral sites are occupied by the small cations. Lithium is preferentially found on octahedral sites that share faces, minimizing electrostatic repulsions between the irons. While in the hexaferrites the structures generally consist of close-packed oxide layers and layers with a BaO_3 composition, rather than the BaO_7 layers used here, other layer compositions are found in more complex compositions. For example, in the $BaO-Fe_2O_3-TiO_2$[34−37] phase field, a large variety of different close-packed layers have been observed, including BaO_7 layers for $BaFe_4Ti_2O_{11}$ and $BaFe_{11}Ti_3O_{23}$,[38] although they are stacked in different sequences. Previous materials isostructural with $BaFe_9LiO_{15}$ displayed magnetic frustration assigned to the presence of triangular motifs within the layers and dominant in-plane antiferromagnetic exchange. The in-plane interactions in $BaFe_9LiO_{15}$ are ferromagnetic and assigned to 90° superexchange interactions, which removes the effect of frustration. The interlayer interactions are dominated by the stronger ∼180° AFM superexchange, and the material has a Néel temperature of ∼460 K. The observed behavior contrasts with that of the early transition metal isostructural analogues in which intralayer AFM direct exchange leads to frustration of the interactions within the layer but is typical of d^5 octahedral systems in close-packed oxide arrays such as MnO and α-Fe_2O_3.[39]

■ ASSOCIATED CONTENT

Ⓢ Supporting Information

Tables of bond angles, representational analysis for the magnetic structure, figures for the Mössbauer analysis, and a cif file for the synchrotron refinement. This material is available free of charge via the Internet at http://pubs.acs.org.

■ AUTHOR INFORMATION

Corresponding Authors

*Department of Chemistry, University of Liverpool, Liverpool L69 7ZD, United Kingdom. E-mail: Claridge@liv.ac.uk .
*Department of Chemistry, University of Liverpool, Liverpool L69 7ZD, United Kingdom. E-mail: m.j.rosseinsky@liv.ac.uk.

Notes

The authors declare no competing financial interest.

■ ACKNOWLEDGMENTS

This work was supported by EPSRC under EP/H000925. We thank the STFC for access to DLS (where Dr. Stephen Thompson and Prof. Chiu Tang are thanked for assistance on beamline I11) and ISIS (where Dr. Winfried Kockelmann is thanked for assistance on GEM).

■ REFERENCES

(1) Tokura, Y.; Seki, S. *Adv. Mater.* **2010**, *22* (14), 1554−1565.
(2) Rao, C. N. R.; Serrao, C. R. *J. Mater. Chem.* **2007**, *17* (47), 4931.
(3) Kimura, T. *Annu. Rev. Mater. Res.* **2007**, *37*, 387−413.
(4) Chu, Y. H.; Martin, L. W.; Holcomb, M. B.; Ramesh, R. *Mater. Today* **2007**, *10* (10), 16−23.
(5) Cheong, S.-W. S.; Mostovoy, M. M. *Nat. Mater.* **2007**, *6* (1), 13−20.
(6) Khomskii, D. I. *J. Magn. Magn. Mater.* **2006**, *306* (1), 1−8.
(7) Eerenstein, W.; Mathur, N. D.; Scott, J. F. *Nature* **2006**, *442* (7104), 759−765.
(8) Pullar, R. C. *Prog. Mater. Sci.* **2012**, *57* (7), 1191−1334.
(9) Turilli, G.; Paoluzi, A. *Ceram. Int.* **1993**, *19* (5), 353−361.
(10) Braun, P. B. *Philips Res. Rep.* **1957**, *12*, 491−548.
(11) Orlov, I.; Palatinus, L.; Arakcheeva, A.; Chapuis, G. *Acta Crystallogr.* **2007**, *B63*, 703−712.
(12) Pollert, E. *Prog. Cryst. Growth Charact.* **1985**, *11* (3), 155−205.
(13) Anderson, J. S.; Hutchison, J. L. *Contemp. Phys.* **1975**, *16* (5), 443−467.
(14) Van Landuyt, J.; Amelinckx, S.; Kohn, J. A.; Eckart, D. W. *Mater. Res. Bull.* **1973**, *8* (10), 1173−1181.
(15) Kitagawa, Y.; Hiraoka, Y.; Honda, T.; Ishikura, T.; Nakamura, H.; Kimura, T. *Nat. Mater.* **2010**, *9* (10), 797−802.
(16) Kimura, T. *Annu. Rev. Mater. Res.* **2007**, *37* (1), 387−413.
(17) Soda, M.; Ishikura, T.; Nakamura, H.; Wakabayashi, Y.; Kimura, T. *Phys. Rev. Lett.* **2011**, *106* (8), 087201.
(18) Ishiwata, S.; Taguchi, Y.; Murakawa, H.; Onose, Y.; Tokura, Y. *Science* **2008**, *319* (5870), 1643−1646.
(19) Kimura, T.; Lawes, G.; Ramirez, A. P. *Phys. Rev. Lett.* **2005**, *94* (13), 137201.
(20) Mignot, J. P.; Isalgué, A.; Obradors, X.; Joubert, J. C.; Tejada, J. *Hyperfine Interact.* **1986**, *28* (1−4), 565−568.
(21) Coelho, A. *TOPAS: Academic, General Profile and Structure Analysis Software for Powder Diffraction Data*, version 4.1, 2007.
(22) Rodríguez-Carvajal, J. *Phys. B (Amsterdam, Neth.)* **1993**, *192* (1), 55−69.
(23) Momma, K.; Izumi, F. *J. Appl. Crystallogr.* **2008**, *41* (3), 653−658.
(24) Müller Buschbaum, H.; Rüter, I. *Z. Anorg. Allg. Chem.* **2004**, *572* (1), 109−114.
(25) Bridges, C. A.; Greedan, J. E.; Kleinke, H. *J. Solid State Chem.* **2004**, *177*, 4516−4527.
(26) Bridges, C. A.; Greedan, J. E. *J. Solid State Chem.* **2004**, *177*, 1098−1110.
(27) Liu, G.; Greedan, J. E. *J. Solid State Chem.* **1996**, *122*, 416−427.
(28) Cuno, E.; Mueller Buschbaum, H. *Monatsh. Chem.* **1989**, *120*, 1−6.
(29) Cuno, E.; Mueller Buschbaum, H. *Z. Anorg. Allg. Chem.* **1989**, *572*, 89−94.
(30) Cuno, E.; Mueller Buschbaum, H. *J. Less-Common Met.* **1989**, *146*, 11−13.
(31) Schiffler, S.; Mueller Buschbaum, H. *J. Less-Common Met.* **1986**, *124*, 229−234.
(32) Schiffler, S.; Mueller Buschbaum, H. *Z. Anorg. Allg. Chem.* **1986**, *542*, 25−30.
(33) de Beaulieu, D. C.; Mueller Buschbaum, H. *Z. Naturforsch., B: Anorg. Chem., Org. Chem.* **1980**, *35*, 669−671.
(34) Vanderah, T. A.; Roth, R. S.; Siegrist, T.; Febo, W.; Loezos, J. M.; Wong-Ng, W. *Solid State Sci.* **2003**, *5* (1), 149−164.
(35) Siegrist, T.; Vanderah, T. A. *Eur. J. Inorg. Chem.* **2003**, *2003* (8), 1483−1501.
(36) Bendersky, L. A.; Vanderah, T. A.; Roth, R. S. *Philos. Mag. A* **1998**, *78* (6), 1299−1328.
(37) Vanderah, T. A.; Loezos, J. M.; Roth, R. S. *J. Solid State Chem.* **1996**, *121* (1), 38−50.
(38) Vanderah, T. A.; Wong-Ng, W.; Toby, B. H.; Browning, V. M.; Shull, R. D.; Geyer, R. G.; Roth, R. S. *J. Solid State Chem.* **1999**, *143* (2), 182−197.
(39) Shull, C. G.; Strauser, W. A.; Wollan, E. O. *Phys. Rev.* **1951**, *83* (2), 333.